Validation of Damage Parameter Based Finite Element Fatigue Life Analysis Results to Combustion Chamber Type TMF Panel Test Results

R. G. Thiede* and J. R. Riccius†

DLR Lampoldshausen, Hardthausen, Germany, D-74239

S. Reese‡

RWTH Aachen University, Aachen, Germany, D-52074

The life of a liquid rocket engine combustion chamber is mainly determined by the extreme temperature gradient and the pressure difference between the hot gas wall and the coolant. A large straining of the hot gas wall due to supressed thermal expansion causes a structural failure after a very low number of cycles during operation. A close to reality experiment with cyclic laser heating and actively cooled Thermo-Mechanical Fatigue (TMF) panels is used to study the material behavior of such rocket engine structures in small scale. A viscoplastic model coupled with isotropic damage, crack-closure effect and thermal ageing is implemented to improve the prediction of life of the TMF panel. The temperature dependent material parameters for isotropic softening, kinematic hardening, stress relaxation, isotropic damage and thermal ageing are optimized while using data from tensile, low cycle fatigue and stress relaxations tests. The number of cycles to failure is determined numerically and compared to experimental measurements of the TMF panel. The damage parameter based finite element analysis predicts the damage initiation point in the middle cooling channel of the TMF panel. Critical damage occurred at the 43^{rd} 900-K-cycle, while the failure of the TMF panel was observed at the 93^{th} 900-K-cycle. Application of the crack-closure effect increases the fatigue life of the TMF panel by 26 cycles and correctly predicts the local thinning phenomenon (the so-called doghouse effect) of the middle cooling channel wall.

Nomenclature

a, b, c	Material parameters for thermal ageing
$b_{1,2}$	Material parameters for isotropic softening
b_{kin}	Material parameter for kinematic hardening
C	Material parameter for kinematic hardening
$\mathcal{C}_{ijkl}$	Elasticity tensor
D, D_c	Isotropic damage, critical damage at crack initiation
E, $\tilde{E}$	Initial Young's modulus, Young's modulus degraded by damage
E_2	Material parameter for kinematic hardening
F	Force
f_{Mises}	von Mises yield function
h	Crack-closure parameter
K	Material parameter for secondary creep
k	Material parameter for isotropic damage
m	Material parameter for viscosity

*Ph.D student, Structures Group, Rocket Engines Department

†Head of Structures Group, Rocket Engines Department, senior AIAA member

‡Professor, Head of Institute of Applied Mechanics

N, N_R	Number of cycles, number of cycles to rupture
n	Material parameter for secondary creep
p, p_D	Accumulated plastic strain, damage threshold
$Q_{0,1,2}$	Material parameters for isotropic softening
R	Drag stress (isotropic softening)
S	Material parameter for isotropic damage
T	Temperature
T_{ij}	Transformation matrix
t, t_{ageing}	Time, ageing time
u	Displacement
X_{ij}	Back stress tensor (kinematic hardening)
Y	Strain energy release rate density
Z	Necking factor

Symbols

α	Thermal expansion coefficient
$\alpha_i, \beta_i, \gamma_i$	Thermal ageing coefficients
Δ	Difference between two scalar values
ε_{ij}	Strain tensor
ε_{ult}, ε_{rup}	Ultimate strain, rupture strain
η	Material parameter for viscosity
γ	Material parameter for kinematic hardening
$\dot{\lambda}$	Plastic multiplier
ν	Poisson ratio
σ_{ij}, $\tilde{\sigma}_{ij}$	Stress tensor, effective stress tensor
σ_{ageing}, σ_{vis}, σ_y	Decreased stress due to thermal ageing, viscous stress, yield stress

Superscripts

c	Creep part
D	Deviatoric part
e	Elastic part
p	Plastic part
p,e	Plastic elastic part
p,i	Plastic inealastic part
θ	Thermal part
$\bar{x}$	Normalization of x
$\dot{x}$	Derivative of x with respect to time ($\mathrm{d}x/\mathrm{d}t$)

The international system (SI) of units is used for all physical quantities, e.g. m, kg, K, s, W.

I. Introduction

THE development of reusable space vehicles is a demanding task especially for designing reliable and durable rocket engines. The rocket combustion chamber is one of the most critical components of a launcher because it is exposed to extremely high thermo-mechanical loads due to its cyclic operation. The actively cooled inner liner is usually made of copper-based alloys and its behavior is mainly governed by low cycle fatigue and creep at elevated temperatures. A cost-efficient experimental setup with a cut-out model of an actively cooled combustion chamber wall (the so-called TMF panel) was developed at the German Aerospace Center (DLR) in Lampoldshausen for validating numerical fatigue life prediction analyses.[1] In the present work, a numerical viscoplastic model coupled with isotropic damage based on the work of Tini[2] is used as a user-defined material in the finite element program package ANSYS. In addition to the work of Thiede,[3] the crack-closure effect is implemented to consider the different stiffness behavior in tensile and compressive direction due to the influence of damage. Uniaxial material tests at different temperatures with and without ageing were performed in order to determine the material parameters for isotropic softening combined with isotropic hardening, kinematic hardening, stress relaxation, thermal ageing and isotropic damage. Finally, the numerically determined number of cycles to failure is compared to experimental data.

II. Experimental Setup

A. TMF Panel

The combustion chamber type TMF panel is a sandwich structure of the copper alloy CuCrZr and galvanically deposited nickel (Fig. 1). CuCrZr is a high conductivity copper-based alloy and surrounds the cooling channels. It is a cost-efficient substitute for NARLoy-Z (CuAgZr) and GRCop-84 (CuCrNb). The small galvanically deposited nickel layer is used at the back side of the TMF panel. With reference to the real full scale engine, this nickel layer represents the nickel jacket which surrounds the inner liner and carries the thrust load of the rocket engine. Furthermore, the TMF panel contains five single fed cooling channels. The active liquid cooling is obtained by a mixture of gaseous and liquid nitrogen. The coolant nitrogen is used for safety reasons despite the real engine is cooled by hydrogen. The nitrogen flow is controlled for each cooling channel separately to avoid thermal blockage in the middle cooling channel as well as to adjust a predefined maximum temperature on the laser loaded side. Note that only the middle cooling channel is representative of one cooling channel in the real combustion chamber throat and the other cooling channels are only needed to restrict the heat flux in transversal direction. A special coating with high absorption on the TMF panel's surface reduces the reflection of infra-red (IR) laser light. The diode laser is heating up the panel surface cyclically and generates a heat flux of 20 MW/m^2 with the 10 mm x 32 mm optics. The thermal, pressure and cooling conditions in the Vulcain engine generate heat fluxes up to 80 MW/m^2.[4] However, the available heat flux of 20 MW/m^2 is assumed to be sufficient for creating validation data for fatigue life analyses of combustion chamber and nozzle throat structures.[1] Finally, small white speckle marks on the surface of the TMF panel allow the measurement of the 3D displacement field with a stereo camera system before, during and after the laser loading.

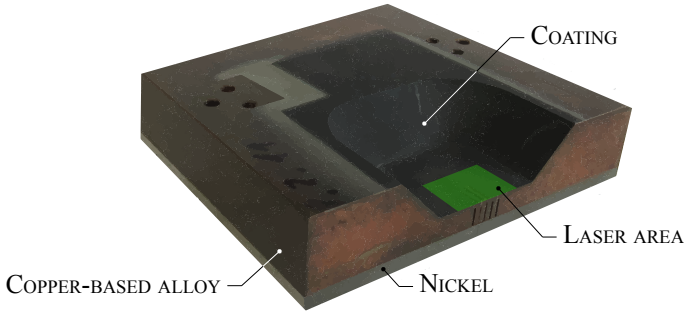

Figure 1. GN_2 outlet half of the TMF panel with cooling channels and coating

B. TMF Test Bench

A cost-efficient experimental test setup for validating numerical prediction analyses with nozzle extension type TMF panels was developed at the German Aerospace Center in Lampoldshausen.[5] This test setup has been modified for studying combustion chamber type TMF panels.[1] The TMF test bench consists of:

- A diode laser with an optical laser power of 11 kW and a wavelength of 940 nm. As depicted in Fig. 1, the surface of the TMF panel is heated locally for many cycles until the structure fails, i.e. a crack occurs on the laser loaded side of the middle cooling channel. A heat flux of 20 MW/m^2 is obtained with the 10 mm x 32 mm optics.

- An IR-camera with a resolution of 640 px x 512 px and a maximum acquisition rate up to 25 Hz in a range of 300 °C to 1500 °C. A narrow band pass filter with a wavelength of 3.99 μm is used to avoid that possible reflections of the laser light could be mis-interpreted as thermal radiation emitted at the surface of the TMF panel. The IR camera is used to measure the 2D thermal field on the laser loaded side of the TMF panel.

- A fluid system that provides nitrogen as a coolant for the laser heated TMF panel. Liquid nitrogen is stored in a 21 m^3 tank. To obtain the target temperature of $T = 160$ K in the TMF panel, gaseous

nitrogen (ambient temperature) and liquid nitrogen (cryogenic temperature) is mixed. The mass flow rate and the pressure in the cooling channels are set by computer controlled valves.

- A 16 MPx stereo camera deformation measurement system in combination with an image correlation software. White speckle marks have to be applied on the coating to measure the 3-component displacement field of the TMF panel surface during the tests.

Further documentation of the TMF test bench can be found in Riccius.[1]

C. Experimental Results

1. Deformation During Hot Run

On the left-hand side of Fig. 2, an image of the coated TMF panel surface with speckle marks is shown. This image is recorded with one camera of the stereo camera system during the hot run. The displacement (u_z) without rigid body motion after one hot run $t_{\text{cycle}} = 600$ s at $T = 900$ K is depicted on the right-hand side of Fig. 2. Obviously, the laser loaded area at the center bulges outwards due to the thermal expansion of the heated structure.

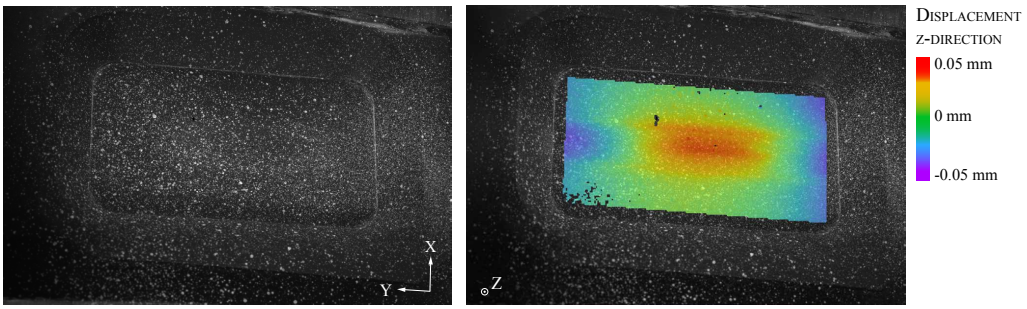

Figure 2. Image with specle marks (left) and deformation measurement result of a hot run (right)

2. Number of Cycles to Failure

The crack in the middle cooling channel of the TMF panel appeared at a total number of 174 cycles. Although only the last 93 cycles are run at a realistic combustion chamber hot run temperature of $T = 900$ K, the TMF panel has shown a fatigue life larger than expected. Possible reasons for the lower number of cycles to failure of real high power core stage combustion chambers like Vulcain are:

- the higher heat flux value in radial direction (≈ 80 MW/m^2) in the nozzle throat cross section of the combustion chamber[4] in comparison to the much lower heat flux in thickness direction of the TMF panel (20 MW/m^2),
- blanching effects (cyclic oxidation and reduction) of the hot gas surface of the chamber wall[6] and
- a localization of the chamber wall material deformation due to an injector distance induced temperature variation in circumferential direction of the combustion chamber wall.[7]

III. Material Model

A. Uniaxial Rheological Model

A viscoplastic model coupled with isotropic damage is used for the fatigue life analysis of the TMF panel.[2] This model is motivated by the classical rheological model for elastoplasticity of Armstrong and Frederick.[8] As depicted in Fig. 3, a viscous dashpot η is added to the model to account for rate-dependent effects.[9]

Furthermore, the one-dimensional isotropic damage variable D is added in order to take into account damage. The so-called effective stress in tension is defined as[10,11]

$$\tilde{\sigma} = \frac{\sigma}{1-D} \tag{1}$$

where the stress-strain relationship for isotropic elasticity is given by $\sigma = \tilde{E}\varepsilon^e$. The total mechanical strain ε is decomposed into its elastic ε^e, plastic-elastic $\varepsilon^{p,e}$ and plastic-inelastic $\varepsilon^{p,i}$ parts by $\varepsilon = \varepsilon^e + \varepsilon^{p,e} + \varepsilon^{p,i}$ (Fig. 3). According to Lion,[12] the plastic-elastic strain $\varepsilon^{p,e}$ can be interpreted as local elastic deformation caused by dislocations and the plastic-inelastic strain $\varepsilon^{p,i}$ as irreversible slip processes on the microscale. The elasticity modulus of the damaged material is expressed as

$$\tilde{E} = E\,(1-D) \tag{2}$$

where E is the elastic spring constant, i.e. the initial Young's modulus. Within the unified framework of isotropic damage, the effective Young's modulus in tension is assumed to be similar to the Young's modulus in compression. For metals the damage measured in compression is smaller than the damage in tension due the closure of microcracks.[11,13] This effect can be modelled by using a scalar crack-closure parameter

$$h = \frac{1-\left(\tilde{E}^+/E\right)}{1-\left(\tilde{E}^-/E\right)} \approx 0.2 \tag{3}$$

where the loading direction is defined for tension $(+)$ and compression $(-)$, respectively. Nonlinear kinematic hardening (with X denoting the back stress) is related to the state of internal microstress concentrations and defines the center of the elastic domain in tension and compression.[11] The back stress X is considered in the model by an elastic spring constant E_2 and a rate independent dashpot $E_2/(\dot{\lambda} b_{\text{kin}})$ where E_2 and b_{kin} are material parameters and $\dot{\lambda}$ the plastic multiplier. Using Perzyna formulation, the plastic multiplier $\dot{\lambda}$ in the simplest case is given by

$$\dot{\lambda} = \frac{\langle f_{\text{Mises}} \rangle}{\eta} \tag{4}$$

where η is a material parameter related to be viscosity of the dashpot. $f_{\text{Mises}} = |\sigma - X| - (\sigma_y + R)$ is the von Mises yield function which includes the initial yield stress σ_y, the stress due to isotropic hardening (with R denoting the drag stress) and the back stress X (Fig. 3). The drag stress R corresponds to the change of the von Mises yield surface and depends on either the dissipated plastic work or the accumulated plastic strain during the loading history.[14] Note that the yield stress σ_y is the stress where irreversible deformation is initiated. The symbol $\langle \cdot \rangle$ defines the Macaulay brackets

$$\langle x \rangle = \begin{cases} 0 & \text{if } x < 0, \\ x & \text{if } x \geq 0. \end{cases} \tag{5}$$

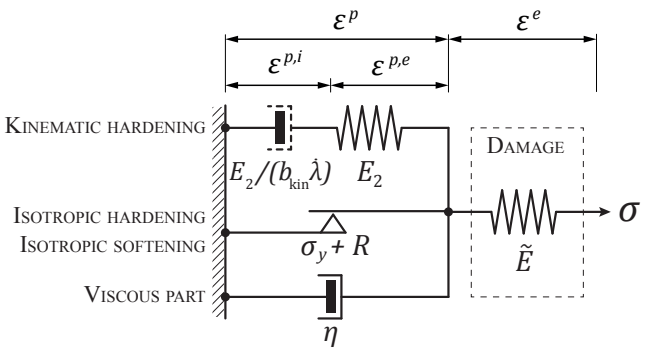

Figure 3. Uniaxial rheological model for viscoplasticity coupled with isotropic damage

B. Continuum Mechanical Approach

On the basis of the extended uniaxial rheological model and the principle of strain equivalence, the constitutive equations for viscoplasticity and isotropic damage with crack-closure effect are generalized in three dimensions. In the small strain regime, the elastic strain tensor is defined as

$$\varepsilon_{ij}^{e} = \varepsilon_{ij} - \varepsilon_{ij}^{p} - \varepsilon_{ij}^{\theta} \tag{6}$$

and in terms of thermo-elasticity ($\varepsilon_{ij}^{p} = 0$)

$$\varepsilon_{ij}^{e} = \frac{1+\nu}{E}\tilde{\sigma}_{ij} - \frac{\nu}{E}\tilde{\sigma}_{kk}\delta_{ij} - \alpha\Delta T\delta_{ij} \tag{7}$$

where ε_{ij} is the total strain tensor, $\varepsilon_{ij}^{p} = \varepsilon_{ij}^{p,e} + \varepsilon_{ij}^{p,i}$ is the plastic strain tensor decomposed into its elastic and inelastic components (Fig. 3), $\varepsilon_{ij}^{\theta}$ is the thermal strain tensor with the scalar thermal expansion coefficient α and the temperature difference $\Delta T = T - T_{\mathrm{ref}}$ and ν is the Poisson ratio. The symbol δ_{ij} defines the Kronecker delta. According to Lemaitre,[13,15] the effective stress with respect to the principle of strain equivalence is defined as

$$\tilde{\sigma}_{ij} = \mathcal{C}_{ijkl}\varepsilon_{ij}^{e} \tag{8}$$

where $\mathcal{C}_{ijkl}$ is the fourth order elasticity tensor. For the stress in the three-dimensional case considering the crack-closure effect, it is difficult to recognize the loading direction (tension or compression) by means of a scalar quantity. Therefore, the effective stress tensor is both transformed into the principal values ($\tilde{\sigma}_{ij}^{\mathrm{diag}}$) and decomposed into its positive $\langle\tilde{\sigma}_{ij}\rangle$ and negative $\langle-\tilde{\sigma}_{ij}\rangle$ part by[11]

$$\tilde{\sigma}_{ij} = T_{ij}\tilde{\sigma}_{ij}^{\mathrm{diag}}T_{ij}^{T} \tag{9}$$

$$\tilde{\sigma}_{ij}^{\mathrm{diag}} = \langle\tilde{\sigma}_{ij}\rangle - \langle-\tilde{\sigma}_{ij}\rangle \tag{10}$$

with

$$\langle\tilde{\sigma}_{ij}\rangle = \begin{pmatrix} \langle\lambda_1^{\tilde{\sigma}}\rangle & 0 & 0 \\ 0 & \langle\lambda_2^{\tilde{\sigma}}\rangle & 0 \\ 0 & 0 & \langle\lambda_3^{\tilde{\sigma}}\rangle \end{pmatrix} \quad \text{and} \quad \langle-\tilde{\sigma}_{ij}\rangle = \begin{pmatrix} \langle-\lambda_1^{\tilde{\sigma}}\rangle & 0 & 0 \\ 0 & \langle-\lambda_2^{\tilde{\sigma}}\rangle & 0 \\ 0 & 0 & \langle-\lambda_3^{\tilde{\sigma}}\rangle \end{pmatrix} \tag{11}$$

where T_{ij} is the orthogonal transformation matrix used for diagonalisation and $\lambda_i^{\tilde{\sigma}}$ are the eigenvalues of the effective stress tensor. Hence, the diagonalised stress tensor of the damaged material considering the crack-closure effect $\sigma_{ij}^{\mathrm{diag}}$ is related to the diagonalised effective stress tensor by

$$\sigma_{ij}^{\mathrm{diag}} = \langle\tilde{\sigma}_{ij}\rangle(1-D) - \langle-\tilde{\sigma}_{ij}\rangle(1-hD) \tag{12}$$

and has to be retransformed into σ_{ij} with T_{ij} using Eq. (9). The evolution law of isotropic damage is expressed as

$$\dot{D} = \sqrt{\frac{2}{3}}\frac{\dot{\lambda}}{1-D}\left(\frac{Y}{S}\right)^{k}\langle p - p_D\rangle \tag{13}$$

where S and k are damage material parameters and p_D is the damage threshold. The damage threshold defines a limit of accumulated plastic strain p where no damage due to microcracks occurs below this limit.[11] The strain energy release rate density is given by

$$Y = \frac{1+\nu}{2E}\left(\frac{\langle\sigma_{ij}\rangle\langle\sigma_{ij}\rangle}{(1-D)^2} + \frac{h\langle-\sigma_{ij}\rangle\langle-\sigma_{ij}\rangle}{(1-hD)^2}\right) - \frac{\nu}{2E}\left(\frac{\langle\sigma_{kk}\rangle^2}{(1-D)^2} + \frac{h\langle-\sigma_{kk}\rangle^2}{(1-hD)^2}\right) \tag{14}$$

with the accumulated plastic strain rate

$$\dot{p} = \sqrt{\frac{2}{3}}\dot{\lambda} \tag{15}$$

For the three-dimensional stress state, the plastic multiplier $\dot{\lambda}$ is computed by using Perzyna formulation[16]

$$\dot{\lambda} = \frac{\langle\bar{f}_{\mathrm{Mises}}^{m}\rangle}{\eta} \tag{16}$$

with the von Mises yield function for viscoplasticity[11]

$$f_{\text{Mises}} = \left|\left|\tilde{\sigma}_{ij}^{D} - X_{ij}^{D}\right|\right| - \sqrt{2/3}\,(\sigma_y + R) = \sigma_{\text{vis}} > 0 \tag{17}$$

and the normalized von Mises yield function

$$\bar{f}_{\text{Mises}} = \frac{\left|\left|\tilde{\sigma}_{ij}^{D} - X_{ij}^{D}\right|\right|}{\sqrt{2/3}\,(\sigma_y + R)} - 1 \tag{18}$$

where m and η are the viscous material parameters, σ_{vis} is the viscous stress, $(\cdot)^D$ denotes the deviatoric part of the tensor corresponding to J_2 flow theory, i.e. viscoplastic strain is governed by the elastic shear energy density.[11] The symbol $||\sigma_{ij}|| = \sqrt{\sigma_{ij}\sigma_{ij}}$ defines the tensor norm. Note that the crack-closure parameter h is not considered in the von Mises yield function as suggested by Desmorat[13] to obtain a convex yield surface. To account for creep strain ε_c in the experimental data, the Norton law

$$\dot{\varepsilon}^c = K\,(\sigma_{\text{vis}})^n \tag{19}$$

is used[17] with K and n are the Norton secondary creep material parameters. The formulation of Perzyna and Norton are coupled by using Eq. (17), Eq. (19) and the formulation of Lemaitre[11] $\dot{\lambda}/(1-D) = \dot{p} = \dot{\varepsilon}^c$ for undamaged material ($D = 0$)

$$K = \frac{1}{\eta} \qquad \text{and} \qquad m = n \tag{20}$$

Isotropic softening results in a decrease of the stress range with the number of cycles. Voce hardening is used in this model for computing the scalar drag stress[18]

$$R = Q_0 p + Q_1\left(1 - e^{(-b_1 p)}\right) + Q_2\left(1 - e^{(-b_2 p)}\right) \tag{21}$$

where $Q_{1,2}$ and $b_{1,2}$ are characterizing the transient slope for small values of the accumulated plastic strain p and Q_0 defines the linear softening behavior for large values of p.

As already mentioned, kinematic hardening was originally described by Armstrong and Frederick and later modified by Chaboche.[8,14] In the present work, the back stress tensor X_{ij} is defined as

$$X_{ij} = \frac{2}{3} C \dot{\varepsilon}_{ij}^{p} - \dot{p}\gamma X_{ij} \tag{22}$$

where $\dot{\varepsilon}^p$ is the plastic strain rate and C and γ are the material parameters for linear kinematic hardening. The links between the kinematic hardening parameters of Chaboche and Armstrong and Frederick which are used in this work are

$$E_2 = C \qquad \text{and} \qquad b_{\text{kin}} = \sqrt{\frac{2}{3}}\gamma \tag{23}$$

where incompressible plastic behavior is assumed.

Thermal ageing is decreasing the material strength over heating time. This effect is included in this model by means of the $1/t$-law with the amplification coefficient a, the time shift parameter b and the stress shift parameter c. These thermal ageing parameters are analytically fitted in order to obtain perfect coincidence for the time points $t_{ageing} = 0$ h, 10 h and 20 h for a given strain ε_i

$$\sigma_{\text{ageing}}\,(\varepsilon_i, t_{\text{ageing}}) = \left(\frac{a}{b + t_{\text{ageing}}}\right) + c \tag{24}$$

The equations for the strain dependent amplification parameter, the time shift parameter and the stress shift parameter are obtained by using the following coefficients for thermal ageing:

$$\begin{aligned} a &= \alpha_1 e^{\alpha_2 \varepsilon} + \alpha_3 e^{\alpha_4 \varepsilon} \\ b &= \beta_1 e^{\beta_2 \varepsilon} + \beta_3 e^{\beta_4 \varepsilon} \\ c &= \gamma_1 e^{\gamma_2 \varepsilon} + \gamma_3 e^{\gamma_4 \varepsilon} \end{aligned} \tag{25}$$

The resulting stress tensor is computed by subtracting the time dependent thermal ageing stress from the stress tensor considering damage. Note that the tensors are subtracted by their principal values to take into account the shear stress.

IV. Material Parameter Identification

A. Test Setup

The tested copper-based alloy CuCrZr is a cost-efficient material with high thermal conductivity which can be applied in rocket combustion chambers. Uniaxial strain-controlled tensile, low cycle fatigue, stress relaxation and dwell tests were performed with cylindrical specimens to obtain the material parameters for elasticity, isotropic softening (for temperatures lower than 900 K also isotropic hardening for the first few cycles), kinematic hardening, stress relaxation, isotropic damage and thermal ageing at different temperature levels (Fig. 4). The measurement uncertainty of the measurement devices for the load F (load cell) and the uniaxial displacement u (extensometer) is class 0.5, i.e. $\Delta F = 0.4$ kN and $\Delta u = 0.5\mathrm{E}^{-4}$ mm, respectively.

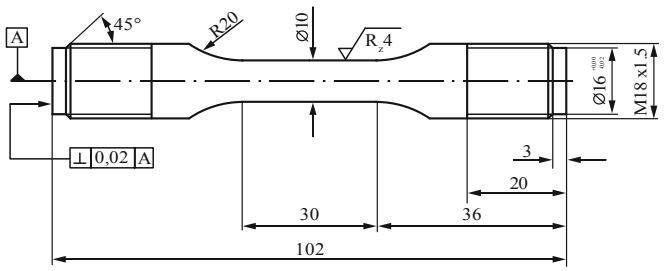

Figure 4. Cylindrical test specimen with dimensions in [mm]

The test setup for identification of material parameters is depicted in Tab. 1. Uniaxial tensile tests are performed at a strain rate of $\dot{\varepsilon} = 0.002$/s at elevated temperatures of $T = \{700\ \mathrm{K}; 900\ \mathrm{K}\}$. Furthermore, thermal ageing is investigated using specimens which were previously heated in an oven for different periods of time $t_{\mathrm{ageing}} = \{0\ \mathrm{h}; 10\ \mathrm{h}; 20\ \mathrm{h}\}$. The uniaxial low cycle fatigue tests are performed with a total strain range of $\Delta\varepsilon = 2\ \%$ and a strain ratio of $\varepsilon_{\mathrm{max}}/\varepsilon_{\mathrm{min}} = -1$ at a strain rate of $\dot{\varepsilon} = 0.002$/s. All cyclic fatigue tests are carried out at temperatures of $T = \{300\ \mathrm{K}; 500\ \mathrm{K}; 700\ \mathrm{K}; 900\ \mathrm{K}\}$ with a trapezoidal loading path. The uniaxial stress relaxation tests are conducted at strain levels increasing from 1 % to 6 % with increments of 1 %, a strain rate of $\dot{\varepsilon} = 0.002$/s and holding periods of $t_{\mathrm{holding}} = 600$ s at temperatures of $T = \{700\ \mathrm{K}; 900\ \mathrm{K}\}$. Uniaxial dwell tests are used to validate the obtained material parameters. The dwell tests are performed with a total strain range of $\Delta\varepsilon = 2\ \%$ and a strain ratio of -1 at a strain rate of $\dot{\varepsilon} = 0.002$/s at elevated temperatures of $T = \{700\ \mathrm{K}; 900\ \mathrm{K}\}$. The holding period at $\varepsilon = \{-1\ \%; +1\ \%\}$ is set to $t_{\mathrm{holding}} = 600$ s.

Table 1. Test setup for identification of material parameters of CuCrZr

Test	$\dot{\varepsilon}$ [1/s]	$\Delta\varepsilon$ [%]	$\varepsilon_{\mathrm{max}}/\varepsilon_{\mathrm{min}}$ [-]	t_{hold} [s]	t_{ageing} [h]	T [K]
Tensile	0.002	-	-	-	0; 10; 20	700; 900
Low Cycle Fatigue	0.002	2	-1	-	0	300; 500; 700; 900
Stress Relaxation	0.002	-	-	600	0	700; 900
Dwell	0.002	2	-1	600	0	700; 900

B. Material Parameter Fitting

The material parameters for the viscoplastic material model coupled with isotropic damage and crack-closure effect are fitted to the experimental data using a nonlinear least squares fit method. The objective function $f(x)$ is defined as the sum of squares of the the stress differences between the true stress value obtained from the experimental data σ_{exp} and the stress values computed by the material model σ_{num} for every time step

$$f(x) = \frac{1}{2}\sum_{i=1}^{N}\left(\sigma(x)_{i,\mathrm{num}} - \sigma(x)_{i,\mathrm{exp}}\right)^2 \tag{26}$$

Both, the MATLAB Optimization Toolbox with the Levenberg-Marquard method and bisquare weights and ANSYS with the conjugated gradients method are used to fit the model's material parameters. Using ANSYS, a finite element model of a quarter of the test sample is applied with a mesh density of 1 element per mm. 3D solid elements with quadratic displacement shape functions (solid186) and uniform reduced integration (keyopt(2)=1) are used in this model. Symmetry boundary conditions are applied at the centered surfaces of the TMF panel. The length of the model is similar to the measurement length l_0 of the extensometer. During the tests, the engineering strain ε_{eng} was measured by an extensometer. Therefore, the applied displacement loading is set by $\Delta l = l_0 \varepsilon_{\text{eng}}$.

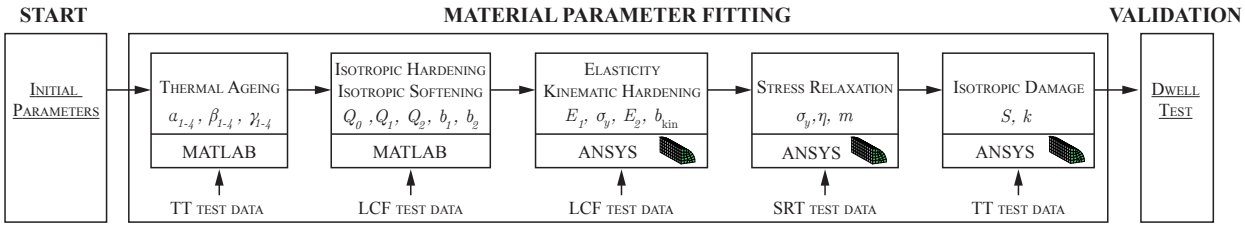

Figure 5. Material parameter fitting approach

The approach of the material parameter fitting procedure is depicted in Fig. 5. Initial parameters are used as input for the optimization procedure. According to Bouajila,[19] isotropic softening, kinematic hardening and stress relaxation are defined using tensile (TT), low cycle fatigue (LCF) and stress relaxation (SRT) test data (Fig. 5). Tensile test data up to a strain limit of $\varepsilon = 5$ % is used to fit the material parameters for the thermal ageing coefficients a_i, b_i and c_i in MATLAB following Eq. (24). The evolution of the drag stress R as a function of the accumulated plastic strain p is fitted in MATLAB using $R = (\Delta\sigma_i - \Delta\sigma_1)/2$ with $i = \{1, \ldots, N_R\}$ where $\Delta\sigma$ is the stress range for each cycle and N_R is the rupture cycle. Note that the isotropic softening parameters $Q_{0,1,2}$ and $b_{1,2}$ remain fixed for the follow-on material parameter fitting procedure in ANSYS. As already mentioned, the method of the conjugated gradients within ANSYS is used for this purpose. Low cycle fatigue test data of the first cycle is used for obtaining the material parameters for elasticity E and σ_y as well as for kinematic hardening E_2 and b_{kin} (Fig. 5). The viscosity parameters η and m are fitted using test data from stress relaxation tests. Prior to the fit of the damage parameters S and k, the damage threshold p_D and the critical damage D_c is defined using tensile and low cycle fatigue data according to Lemaitre.[15] Tensile test data is used to model the evolution of damage starting from $D(\varepsilon_{\text{ult}}) = 0 \rightarrow D(\varepsilon_{\text{rup}}) = D_c$ where ε_{ult} is the ultimate strain and ε_{rup} is the rupture strain. Finally, a dwell test (DW) is applied to validate the fitted material parameters for the viscoplastic model coupled with isotropic damage and crack-closure effect.

C. Comparison of the Numerical Analysis Results to Experimental Data

1. Tensile Test

Results of tensile tests with uniaxial specimens that were carried out at $t_{\text{ageing}} = \{0\text{ h}; 10\text{ h}; 20\text{ h}\}$ and $T = \{700\text{ K}; 900\text{ K}\}$ are used to fit the thermal ageing coefficients. The difference of stress for a constant strain level $\varepsilon = \{1\ \%; 2\ \%; \ldots; 5\ \%\}$ between the aged specimens at $T = 900$ K is shown in Fig. 7. It can seen that the fit of the reduction of the stress due to thermal ageing shows a good agreement. Thermal ageing up to $T = 700$ K is neglected.

2. Low Cycle Fatigue Test

Low cycle fatigue test data is used to fit the isotropic softening and the kinematic hardening behavior for different temperature levels $T = \{300\text{ K}; 500\text{ K}; 700\text{ K}; 900\text{ K}\}$ as well as for obtaining the damage threshold parameter p_D. Results of the isotropic softening material parameter fit are shown on the right-hand side of Fig. 7. Obviously, isotropic hardening can be observed for small values of the accumulated plastic strain p at $T = \{300\text{ K}; 500\text{ K}; 700\text{ K}\}$. Linear isotropic softening for large values of p at all temperatures is observed for all considered temperatures. This effect is governing the material behavior of CuCrZr regarding the TMF panel tests.

For the first low cycle fatigue test cycle the model's prediction of the elasticity and kinematic hardening at a strain range of $\Delta\varepsilon = 2$ % and a strain rate of $\dot{\varepsilon} = 0.002/\mathrm{s}$ at $T = \{300\ \mathrm{K}; 500\ \mathrm{K}; 700\ \mathrm{K}; 900\ \mathrm{K}\}$ is shown in Fig. 8. The test results obtained in the first quarter cycle ($0\ \% \leq \varepsilon \leq 1\ \%$) are not taken into account for the material parameter fit. Instead, the first full cycle ($-1\ \% \leq \varepsilon \leq 1\ \%$) is used for fitting the material parameters. In Fig. 8, the plastic slope of the full cycle shows a good agreement with experimental data at all temperatures. Regarding the first quarter, the plastic slope for $T = 300$ K and 500 K is not well reproduced by the model.

According to Lemaitre,[11] the isotropic damage material parameters S, k, D_c and p_D are identified by using tensile and low cycle fatigue data.[15] In Fig. 6, the evolution of isotropic damage in compression without crack-closure effect relating to Eq. (2) is plotted. The damage threshold p_D should be the limit of accumulated plastic strain where damage starts to evolve. The crack-closure parameter is taken from Lemaitre and set to 0.2.

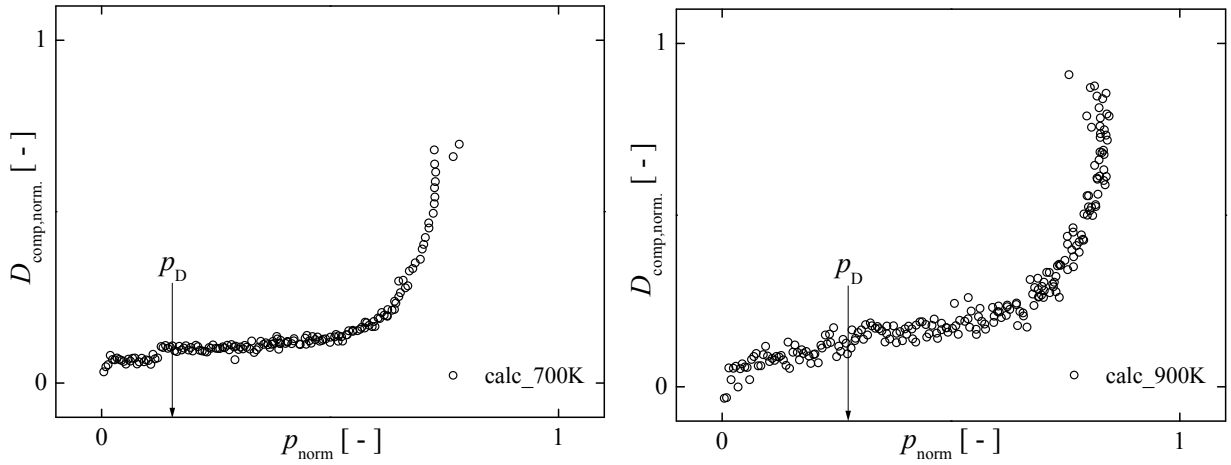

Figure 6. Calculated uniaxial isotropic damage (Eq. 2) over all cycles for different temperatures

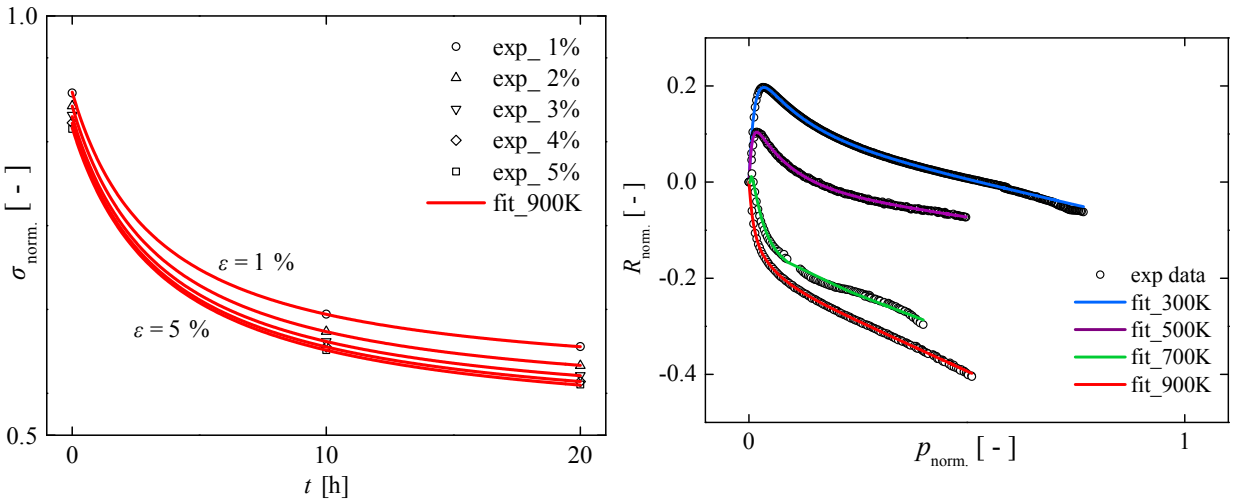

Figure 7. Simulation of thermal ageing (left) and isotropic softening behavior (right)

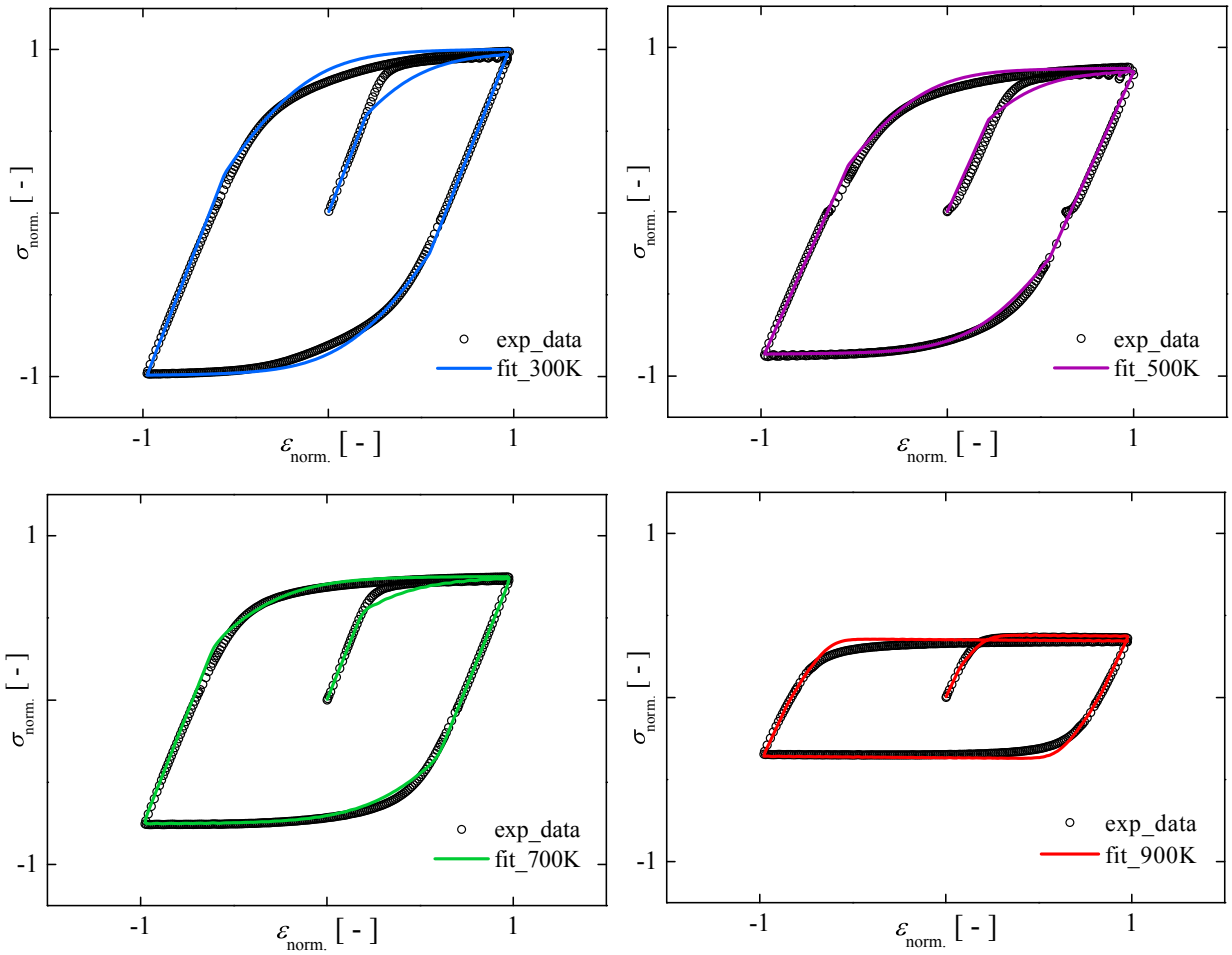

Figure 8. Simulation of kinematic hardening behavior for different temperatures

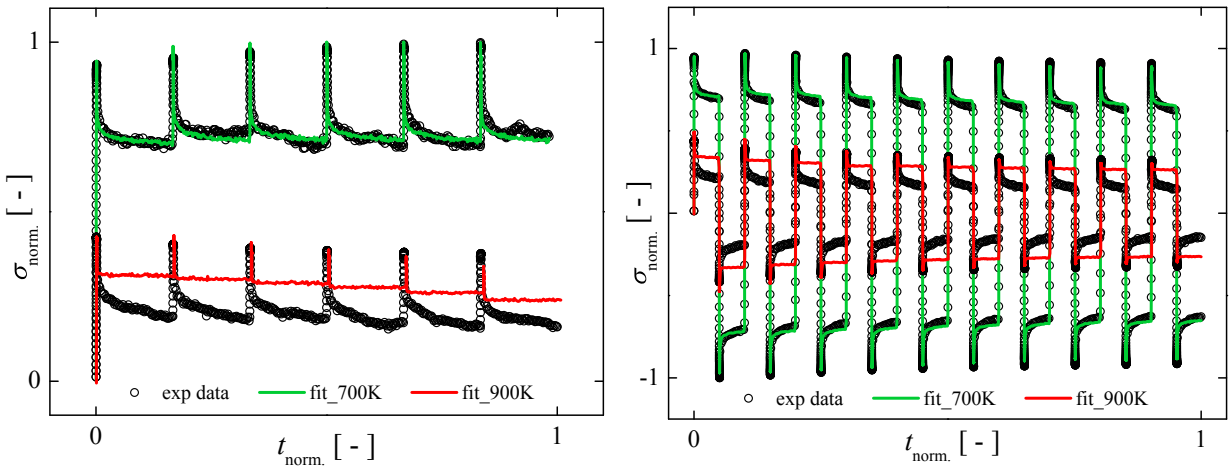

Figure 9. Simulation of stress relaxation behavior (left) and dwell test for validation purposes (right)

3. Stress Relaxation Test

Stress relaxation test data at $T = 700$ K and 900 K is used to investigate the relaxation of the stress at constant strain levels of $\varepsilon = \{1\ \%; \ldots; 6\ \%\}$ with increments of $\Delta\varepsilon = 1\ \%$ and constant holding periods of $t_{\text{holding}} = 600$ s. The holding period is similar to the laser heating period of the TMF panel. As shown on the left-hand side of Fig. 9, a good coincidence between the fit and the experimental data of $T = 700$ K is obtained and saturation of the viscous stress at $t_{\text{holding}} = 600$ s is observed. Furthermore, a linear decrease of viscous stress during the holding period is observed in the experimental data at $T = 900$ K. It can seen that the fit saturated rapidly and the decreased stress level is not reached entirely by the model prediction.

4. Dwell Test

For validating the fitted material parameter set, dwell tests with an identical holding period of $t_{\text{holding}} = 600$ s in tension and compression, an identical strain rate of $\dot{\varepsilon} = 0.002/\text{s}$ and a constant strain range of $\Delta\varepsilon = 2\ \%$ at the same temperature levels $T = \{700\ \text{K}; 900\ \text{K}\}$ are performed. The model's prediction shows a good agreement with the experimental data at $T = 700$ K (Fig. 9). This applied material parameter set is used for the structural analysis of the TMF panel.

V. Finite Element Model

A. Mesh

The finite element mesh of the TMF panel consists of 3D solid elements (hexahedrons) with linear displacement shape functions (solid185). Selective reduced integration ($\bar{B}$ method) is applied to avoid shear and volumetric locking effects.[20] Shear locking can occur in fully integrated lower order elements. In case of fully incompressible material behavior in combination with fully integrated elements, volumetric locking could occur too. Both effects are leading to a stiffer material response. Furthermore, only half of the domain of the TMF panel is modeled and the elements are stretched in longitudinal direction to reduce the computational effort significantly (Fig. 10). As shown in Fig. 10, a structured fine mesh with a mesh density of 4 elements per mm is used in the critical cross-section of the TMF panel where damage is mainly expected. The total number of nodes is 74k and the total number of elements is 65k for the applied mesh.

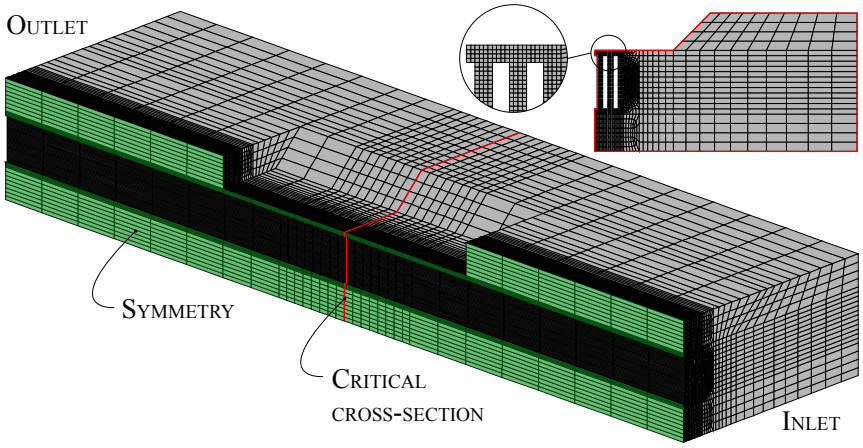

Figure 10. Finite element mesh of the TMF panel with critical cross-section

B. Thermal Analysis

Three steady state static thermal finite element analyses are performed to compute temperature fields for the follow-on quasi static structural analysis. The heating of the TMF panel by the laser beam is taken into account by a heat flux boundary condition. The cooling (GN_2) of the TMF panel is taken into account by boundary conditions with a constant film coefficient at all of the inner surfaces of the cooling channels.

Therefore, a single film coefficient is fitted for each temperature $T = \{680\ \text{K}; 750\ \text{K}; 900\ \text{K}\}$ with the objective to obtain the maximum temperature on the laser loaded surface of the TMF panel as measured with the IR-camera during TMF tests. The inlet temperature of the TMF panel is set to $T = 160$ K using convection, too. The temperature dependent emissivity of the coated surface with high absorption is also taken into account in the thermal analyses by applying radiative boundary conditions.

C. Structural Analysis

1. Boundary Conditions

Symmetry boundary condition is applied at the intersection area of the TMF panel (Fig. 10). In order to take into account the mounting of the TMF panel, the inlet surface is fixed in longitudinal direction. This prevents a rigid body translation and a rigid body rotation without restraining the bending of the TMF panel caused by different thermal expansion coefficients of the two TMF panel materials nickel and CuCrZr (the so-called bimetal effect). As already mentioned, the pressure in the cooling channels at inlet and outlet and the maximum temperature on the laser loaded side is measured continuously during the TMF tests. Both, a temperature field and a uniform pressure are applied similarly to the experimental test conditions for each cycle.

2. Solution Settings

For the quasi static structural analysis, large-deflection effects are included to take into account the bimetal effect of the TMF panel during pre-cooling ($T_{\text{cold}} = 160$ K). The time step for the cooling after each laser loading cycle is set to $\Delta t_{\text{cold}} = 100$ s within the quasi static analysis. As shown in Fig. 11, the main cycle of a TMF panel test consists of four load steps:

1. Laser loading ramped up from T_{cold} to T_{max} over a period of $t_1 = 10$ s
2. Laser continously on at T_{max} for $t_2 = 590$ s to account for thermal ageing and stress relaxation (steady state hot run)
3. Laser loading ramped down from T_{max} to T_{cold} over a period of $t_3 = 99$ s
4. Laser off at T_{cold} for $t_4 = 1$ s (steady state post-cooling)

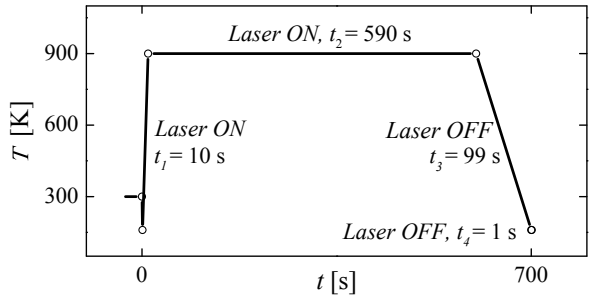

Figure 11. Hot run of one cycle at $T_{\text{max}} = 900$ K

As already mentioned, the crack in the middle cooling channel of the TMF panel appeared at 174 cycles. During the TMF test, the 1st cycle is run at $T = 680$ K, 80 cycles are run at $T = 750$ K and only the last 93 cycles are run at a realistic combustion chamber hot run temperature of $T = 900$ K. Riccius[1] showed that damage can be neglected during the first 81st cycles (usage factor below 5 %). Therefore, only one cycle at $T = 680$ K and one cycle at $T = 750$ K is computed in the structural analysis and the damage threshold is reduced by the difference of 79 cycles at $T = 750$ K. This accelerated approach reduces significantly the computation time.

3. Numerical Analysis Results: Deformation During Hot Run

In Fig. 12, the experimentally obtained and numerically determined out of plane displacement of the measurement point during one hot run at $T = 900$ K is shown. The measurement point is placed on the center of the middle cooling channel's laser loaded surface. Rigid body rotation due to the bimetal effect is included in the experimental data. Note that the initial displacement u_0 is subtracted from each displacement u_i using $u_{\text{relative}} = u_i - u_0$.

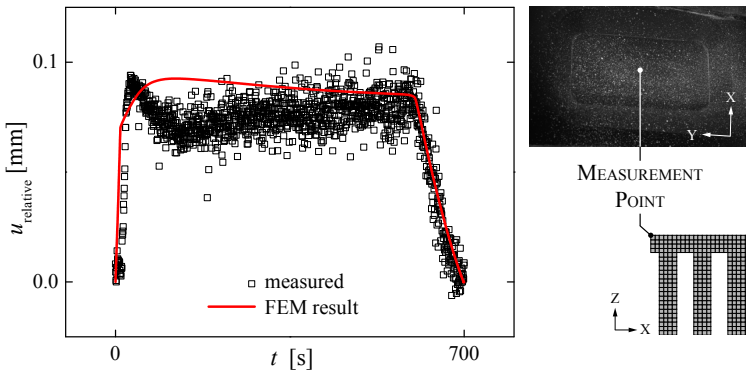

Figure 12. Comparison of the relative displacement during hot run at $T_{\max} = 900$ K

Regarding the experimental data, a maximum relative displacement of the measurement point $u_{\max} = 0.094$ mm is obtained at $t = 10$ s. Then, the displacement decreases and reaches saturation with an averaged value of $\bar{u}_z \approx 0.084$ mm at the end of the steady state hot run at $t = 600$ s. This is caused by the bimetal effect. At the end of the hot run, the displacement of the measurement point is decreasing linearly to the initial state at $t = 699$ s. The measurement uncertainty of the experimental data is $\Delta u = \pm 0.5$E-3 mm. The numerical solution slightly deceeds the maximum displacement of the first peak by $\Delta u_{\max} = 1.3$E-3 mm and slightly exceeds the saturated displacement by $\Delta \bar{u} = 1.5$E-3 mm. Note that activation of nonlinear energy stabilization in ANSYS for the first substep of steady state hot run ($t_2 = 590$ s) is needed to reproduce the bimetal effect of the TMF panel correctly. Another important aspect, the periodical decrease of the laser power is set similar to the TMF panel test ($t_3 = 99$ s). This cooling period has a large influence on the numerical result and the doghouse failure, respectively.

4. Numerical Analysis Results: Number of Cycles to Failure

The structural damage parameter based finite element analysis of the TMF panel shows that the critical damage D_c is reached during the 43$^{\text{rd}}$ hot run of the $T_{\max} = 900$ K loading phase of the TMF panel. This is an underestimation of the experimental result (93 cycles at 900 K) by nearly 54 %. The distribution of the isotropic damage of the numerically predicted failure cycle of the TMF panel is depicted on the left-hand side of Fig. 13. The damage evolution D_{P3} with respect to the number of hot run cycles ($T = 900$ K) at node P3 is shown on the right-hand side of Fig. 13. It can be seen that the crack-closure parameter h leads to a smaller damage accumulation in comparison to the reference case without crack-closure effect ($h = 1$).

In Fig. 14, the transversal stress σ_x depending on the transversal mechanical strain ε_x is depicted for several cycles at the three nodes P1, P2 and P3. Obviously, all three points are subjected to an increasing compressive deformation (in transversal direction of the TMF panel). The initial strain range in transversal direction of one cycle at $T = 900$ K without damage is $\Delta \varepsilon_x \approx 10$ % and decreases cyclically due to the influence of damage.

VI. Conclusion

In addition to the work of Thiede,[3] the crack-closure effect is implemented into the isotropic damage framework and applied to the structural analysis. The material parameters are fitted with ANSYS using a detailed model of a quarter of the specimen. Kinematic hardening, isotropic softening (for temperatures lower than 900 K combined with initial isotropic hardening) and viscosity is well represented. With the fitted parameters, dwell tests are numerically analyzed to validate the applied material parameter set at

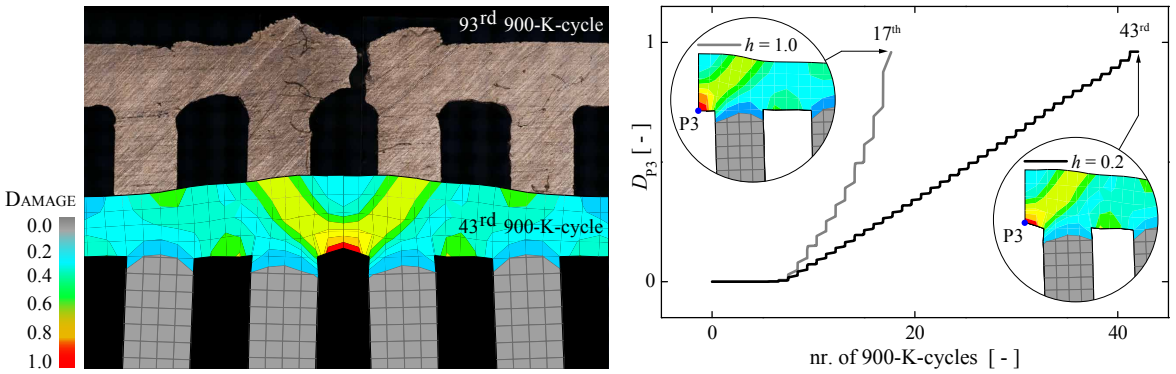

Figure 13. Comparison of experimental and numerical deformation result with damage distribution (left) and damage evolution at node P3 with ($h = 0.2$) and without ($h = 1.0$) crack-closure effect (right)

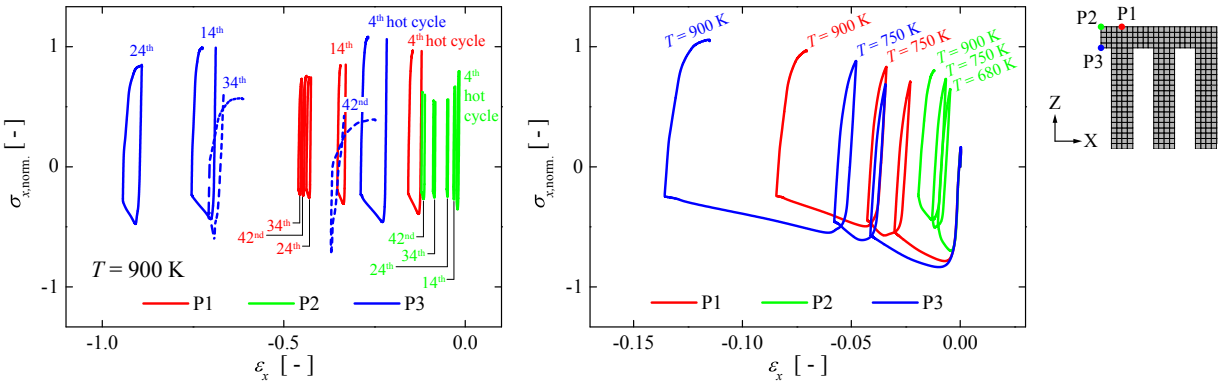

Figure 14. Transversal stress in dependency of transversal mechanical strain for the hot run cycles $n_{\mathrm{hot}} = \{4^{\mathrm{th}}; 14^{\mathrm{th}}; 24^{\mathrm{th}}; 34^{\mathrm{th}}; 42^{\mathrm{nd}}\}$ at $T = 900$ K (left) and for 1^{st} to 3^{rd} cycle (right)

$T = \{700\ \mathrm{K}; 900\ \mathrm{K}\}$. The model prediction shows a good agreement with experimental data. The application of this material parameter set in combination with the crack-closure effect shows that the experimentally observed thinning of the middle cooling channel wall (the so-called doghouse effect) is reproduced well. Furthermore, the number of cycles to failure during the hot run at $T = 900$ K increased by 26 cycles using the crack-closure parameter $h = 0.2$.

The results imply, that the applied viscoplastic model coupled with isotropic damage and crack-closure effect can be used for a conservative fatigue life prediction of rocket combustion chamber type structures.

VII. Outlook

The material parameters for the damage based material model are obtained from both, low cycle fatigue tests at $T = \{300\ \mathrm{K}; 500\ \mathrm{K}; 700\ \mathrm{K}; 900\ \mathrm{K}\}$ and tensile and stress relaxation tests at $T = \{700\ \mathrm{K}; 900\ \mathrm{K}\}$. In addition, dwell tests at $T = \{700\ \mathrm{K}; 900\ \mathrm{K}\}$ are used to validate the final material parameter set. The application of a static recovery factor for the kinematic hardening could result in a better coincidence of the numerically determined stress relaxation at $T = 900$ K.[21] Classical creep tests at high temperatures as well as tensile and low cycle fatigue tests at cryogenic temperatures (e.g. $T = 160$ K) would lead to an extended material parameter set. This extended material parameter set could cover more precisely the conditions during a TMF panel test and especially the damage behavior at cryogenic temperature during cooling.

Isotropic damage with crack-closure effect is used within the material model for the structural analysis. Defining anisotropic properties of the TMF panel material that take into account the variation of the microscopic structure within the rolled sheet could help to improve the numerical analysis results.

Furthermore, a one-way coupling of the steady state thermal analysis and the follow-on quasi static

structural analysis of the rocket combustion chamber type TMF panel has been performed. A CFD analysis of the coolant flow in combination with a transient thermal analysis could help to take into account both, capacitive cooling of the structure as well as a variation of the coolant film coefficient due to the heating of the coolant of the TMF panel.

In addition, larger computational resources would allow a finer mesh size in the laser loaded cross section of the TMF panel. A finer mesh could help to investigate the mesh dependency of the damage model.

Finally, a larger number of TMF tests with different holding periods at different temperature levels in combination with different materials should be performed to confirm and improve the numerical determined results.

Acknowledgments

The authors would like to acknowledge Vivian Tini for programming the isotropic damage model source code within the finite element program FEAP, Wissam Bouajila for his support concerning the definition of the material parameters for stress relaxation, kinematic hardening, isotropic softening and Andreas Gernoth and Ingo Dörr for the TMF panel test setup.

References

[1]Riccius, J. R., Bouajila, W., and Zametaev, E. B., "Comparison of finite element analysis and experimental results of a combustion chamber type TMF panel test," *AIAA 2013-3846*, 2013.

[2]Tini, V., Vladimirov, I. N., and Reese, S., "Lifetime prediction of rocket combustion chamber wall by means of viscoplasticity coupled with ductile isotropic damage," *ASME 2012 11th Biennial Conference on Engineering Systems Design and Analysis*, American Society of Mechanical Engineers, 2012, pp. 497–502.

[3]Thiede, R. G., Zametaev, E. B., Riccius, J. R., Fassin, M., and Reese, S., "Comparison of damage parameter based finite element fatigue life analysis results to combustion chamber type TMF panel test results," *AIAA 2015-4070*, 2015.

[4]Preclik, D., Wiedmann, D., Oechslein, W., and Kretschmer, J., "Cryogenic rocket calorimeter chamber experiments and heat transfer simulations," *AIAA 1998-3440*, 1998.

[5]Gernoth, A., Wurdak, M., Riccius, J. R., Schlechtriem, S., Wiedmann, D., Schwarz, W., and Brummer, L., "TMF test based validation of numerical methods for the analysis of heat-loaded walls," *AIAA 2010-6887*, 2010.

[6]Duval, H., Lefez, B., da Silva B, T., Inglebert, G., and Begoc, S., "Experimental investigation of blanching effects of typical rocket combustion chamber wall materials," *5th European Conference for Aeronautics and Space Sciences (EUCASS), Munich*, 2013.

[7]Watanabe, D., Imai, K., Ogawara, A., Kawatsu, K., Negishi, H., Daimon, Y., Tani, N., Yamanishi, N., Sunakawa, H., and Kurosu, A., "Cooling Analysis for rocket engine combustion chamber with high fidelity simulation," *AIAA 2013-3844*, 2013.

[8]Frederick, C. O. and Armstrong, P. J., "A mathematical representation of the multiaxial Bauschinger effect," *Materials at High Temperatures*, Vol. 24, No. 1, 2007, pp. 1–26.

[9]Kowollik, D., Tini, V., Reese, S., and Haupt, M., "3D fluid–structure interaction analysis of a typical liquid rocket engine cycle based on a novel viscoplastic damage model," *International Journal for Numerical Methods in Engineering*, Vol. 94, No. 13, 2013, pp. 1165–1190.

[10]Kachanov, L. M., "Rupture time under creep conditions," 1958, pp. 26–31.

[11]Lemaitre, J., *A course on damage mechanics*, Springer, 1992.

[12]Lion, A., "Constitutive modelling in finite thermoviscoplasticity: a physical approach based on nonlinear rheological models," *International Journal of Plasticity*, Vol. 16, No. 5, 2000, pp. 469–494.

[13]Desmorat, R. and Cantournet, S., "Modeling microdefects closure effect with isotropic/anisotropic damage," *International Journal of Damage Mechanics*, 2007.

[14]Chaboche, J. L., "Constitutive equations for cyclic plasticity and cyclic viscoplasticity," *International Journal of Plasticity*, Vol. 5, No. 3, 1989, pp. 247–302.

[15]Lemaitre, J. and Desmorat, R., *Engineering damage mechanics: ductile, creep, fatigue and brittle failures*, Springer, 2005.

[16]Perzyna, P., "Fundamental Problems in Viscoplasticity," *Advances in Applied Mechanics*, Vol. 9, 1966, pp. 243–377.

[17]Norton, F. H., *The creep of steel at high temperatures*, No. 35, McGraw-Hill Book Company, 1929.

[18]Voce, E., "The relationship between stress and strain for homogeneous deformation," *Journal of the Institute of Metals*, Vol. 74, 1948, pp. 537–562.

[19]Bouajila, W. and Riccius, J. R., "Identification of the unified Chaboche constitutive model's parameters for a cost efficient copper-based alloy," *Space Propulsion Conference, Cologne*, 2014.

[20]Hughes, T. J. R., "Generalization of selective integration procedures to anisotropic and nonlinear media," *International Journal for Numerical Methods in Engineering*, Vol. 15, No. 9, 1980, pp. 1413–1418.

[21]Schwarz, W., Schwub, S., Quering, K., Wiedmann, D., Höppel, H., and Göken, M., "Life prediction of thermally highly loaded components: modelling the damage process of a rocket combustion chamber hot wall," *CEAS Space Journal*, Vol. 1, No. 1-4, 2011, pp. 83–97.